
Abstract

Theoretical condensed matter research is plagued by a fundamental issue of complexity. The sheer amount of degrees of freedom in a material on any technologically relevant scale is overwhelming (e.g. $\sim 10^{23}$ electrons per cm^3), and makes it impossible to describe the quantum mechanical wavefunction exactly.

The Hamiltonian plays a central role in the description of crystals, the subject of this thesis. It can be decomposed into various parts, and their interactions. Depending on the physics under scrutiny it then often suffices to solve only one of those parts. This can be either because the energy scales and associated timescales that govern the constituents are very different, or because the interactions between them are small. One example, often put into practice, is the separation of electronic and phononic (lattice) degrees of freedom, leading to the well-known Born-Oppenheimer approximation, decoupling their respective motion. Another is the often neglected spin-orbit coupling, due to the tiny prefactor associated with its relativistic origin.

Solving these subproblems then allows for progress to be made in understanding the physics that governs them. However, there will inevitably be systems for which this interaction is not small and leads to fascinating new physics that manifestly depends on both subsystems combined. In this thesis we focus on these cases and how they arise in functional materials, with the occasional eye towards applications in technology.

The reason why these cross-order couplings can be interesting for technological applications, is that often one of the orders is more robust with respect to perturbations, and therefore more long-lived, but also harder to control efficiently. By exploiting the cross-order coupling in certain materials, one could potentially control the long lived order by applying perturbations to the more easily controllable order.

In giant Rashba effect systems, the coupling between spin and ferroelectric order leads to a linear spin-splitting of the band structure, whose sign depends on the orientation of the ferroelectric polarization. We show that, rather than the relativistic Rashba effect, a combination of electrostatics and atomic spin-orbit coupling lies at the origin of the large splitting.

The coupling between magnetism and ferroelectricity in multiferroic GdMn_2O_5 leads to a never before observed four-state hysteresis loop for the ferroelectric polarization, which depends on the magnitude, angle and history of the applied magnetic field. As we will show, this four-state hysteresis loop is accompanied by a full 360° rotation of spins in the material, which resembles the crankshaft of a car, converting the linear back-and-forth motion of the magnetic field into a rotational motion of the spins.

In a thin film of elemental Chromium, the ultrafast dynamics of a spin density wave, coupled to a slower varying charge density wave, allows for a high degree of control of the latter through excitations of the former. This allows us to predict the sequence of optical pulses to be applied to the material in order to follow closely an enveloping signal function.

And finally, the coupling between ferroelectricity and strain in BaTiO_3 leads to a softening at purely ferroelectric domain walls, allowing for some mechanical control of the position of this wall.

We utilize both theoretical and computational tools to understand the nature of these interactions, how they lead to cross-order coupling in these materials, and how this then translates into the experimentally observed behavior.

Contents

1	Spin-momentum locking in high spin-orbit coupled ferroelectrics	5
1.1	Introduction	5
1.2	Rashba-Bychkov Effect	7
1.3	Orbital Rashba Effect	9
1.3.1	Tight-Binding model	10
1.4	Germanium Telluride	14
1.5	Methods	16
1.6	Results and Discussion	18
1.7	Conclusions	20

Chapter 1

Spin-momentum locking in high spin-orbit coupled ferroelectrics

1.1 Introduction

The research field of spintronics aims to understand the behavior of spins inside materials, and translate this understanding into active control of these degrees of freedom for possible technological applications [**Joshi2016**]. Many devices have been theorized, for example, spin field-effect transistors (spin-FET)[**Datta1990**], and storage devices which utilize spin-current and associated spin-transfer torque to efficiently manipulate magnetic domains [**Kent2015**], both in ferromagnets [**Nunez2011**], and antiferromagnets [**Jungwirth2016**]. In spite of fundamental interest and potential for applications, the actual realization of these spin-FET devices has been rather elusive. One of the main culprits for the limited success to date is that the devices require very granular, ideally electric, control of the spin. This is often precluded by the widely separated energy scales and weak coupling between magnetic and charge degrees of freedom. One class of materials that can allow for such electric control of spin-polarized states are the ferroelectric semiconductors with large atomic spin-orbit coupling (SOC) [**Picozzi2014**, **DiSante2013**, **Ishizaka2011**, **Kim2014**]. Inversion symmetry breaking together with SOC results in a linear energy splitting of spin-polarized bands, manifested in the bulk band structure as a conical intersection surrounding a time-reversal symmetric point of the Brillouin Zone (BZ) (see Fig. 1.1). Due to the definite spin-polarization of these bands, current carriers ¹ traveling through the material will tend to align their spins to this spin-polarization. As we discuss in more detail in the following, the direction of the spin polarization depends on the orientation and strength of the electric field \mathbf{E} . In ferroelectrics, an internal field results from polarization P and associated electric dipole moments, allowing it to be tuned and switched by an external electric field. These spin-polarized states have been observed both experimentally [**Ishizaka2011**, **Liebmann2016**, **Krempasky2015SurfaceSemiconductor**], and from *ab-initio* density functional theory (DFT) simulations [**DiSante2013**]. It is, however, often not well understood and misattributed what the underlying microscopic mechanisms are that lead to the observed splitting.

We start by investigating multiple origins of this \mathbf{k} and \mathbf{E} dependent spin-

¹holes in the case of Fig. 1.1

splitting. The discussed energy contributions all arise due to the Hamiltonian of form

$$H_R(\mathbf{k}) = \alpha_R \frac{\mathbf{E}}{|\mathbf{E}|} \cdot (\mathbf{k} \times \hat{\boldsymbol{\sigma}}), \quad (1.1)$$

where $\hat{\boldsymbol{\sigma}}$ is the electron spin operator, and \mathbf{E} the electric field. It will turn out that multiple microscopic effects can lead to contributions of this form, some of these are well known, others are more obscure. The magnitude of the contribution depends on these microscopics, namely whether the effect is purely relativistic or rather a combination of relativistic and electrostatic terms.

Certain materials demonstrate an exceedingly big splitting, for example in Germanium Telluride (GeTe) as can be seen in Fig. 1.1. We therefore use this material as the main illustration throughout this chapter. To investigate how these effects occur in GeTe, we utilize DFT followed by a Wannierization in order to get an idea of the local, real-space, properties of the Bloch functions around the time reversal symmetric points of the BZ where the linear splitting occurs.

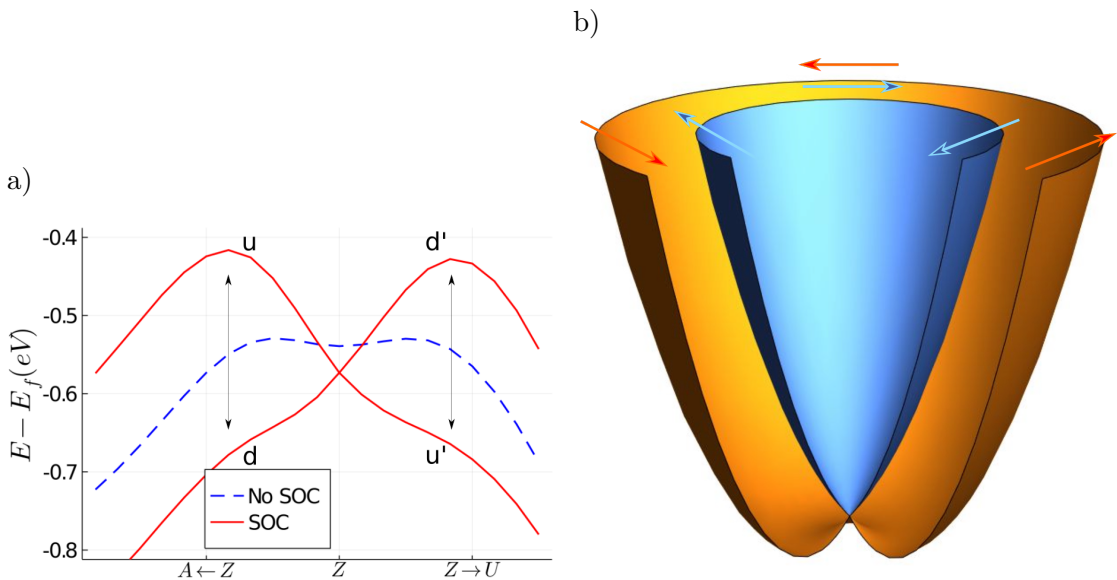


Figure 1.1: **Large Rashba splitting** (a) The band dispersion of the first valence band in GeTe around the Z -point of the Brillouin zone (see Fig. ?? for details). Two graphs show both non spin-orbit coupled (NSOC, blue), and spin-orbit coupled (SOC, red) case. The $u - d$ and $u' - d'$ labels designate the up and down spin-polarized bands, where the prime signifies that the orientation of the spin quantization axis depends on \mathbf{k} . b) Shifted parabolic energy levels due to Rashba splitting, and associated spin texture indicated by the arrows.

We finish with a conclusion on the origin of most observed Rashba-like phenomena [could be better].

1.2 Rashba-Bychkov Effect

The first discovered, and most well known effect bearing the form of Eq. 1.1 is the Rashba-Bychkov effect, first derived in their seminal 1959 paper [**Rashba1959SymmetryAr**]. It is a purely relativistic effect that is derived from an expansion to second order in $1/c$, c denoting the speed of light, of the electronic Dirac equation (where the Fouldy-Wouthuysen transformation was applied):

$$\mathcal{H} |\psi\rangle = \left[\frac{\mathbf{p}^2}{2m} - eV - \frac{e\hbar}{4m^2c^2} (\boldsymbol{\sigma} \cdot [\nabla V \times \mathbf{p}]) - \frac{\hbar^2}{8m^2c^2} \Delta V - \frac{\mathbf{p}^4}{8m^3c^2} \right] |\psi\rangle = E |\psi\rangle \quad (1.2)$$

where ψ is a two component spinor, V denotes the electric potential, $\boldsymbol{\sigma}$ a vector of Pauli-matrices ($\sigma_x, \sigma_y, \sigma_z$), m and e the electron mass and charge respectively, and \mathbf{p} the canonical momentum. The first two terms are the non-relativistic part of the Hamiltonian, the third one represents the SOC, the fourth is known as the Darwin effect and the fifth is the relativistic correction to the effective electron mass. As is common in literature, we introduce the spin-orbit coupling constant $\lambda = \frac{e\hbar}{4m^2c^2}$. In a crystal with a periodic potential $V(\mathbf{r})$, the electronic wavefunctions are Bloch wavefunctions $|\psi_n^k\rangle = e^{i\mathbf{k}\cdot\mathbf{r}} |u_n^k(\mathbf{r})\rangle$, where u_n denotes the cell-periodic part, and n is the band index. In the following we drop \mathbf{r} in the wavefunctions, and inner products are assumed to be integrated over all space. To obtain the eigenvalue equation for $|u_n^k\rangle$, we insert $|\psi_n^k\rangle$ in Eq. 1.2, and carry out the differentiation $\mathbf{p} e^{i\mathbf{k}\cdot\mathbf{r}} |u_n^k\rangle = e^{i\mathbf{k}\cdot\mathbf{r}} (\mathbf{p} + \mathbf{k}) |u_n^k\rangle$, and similarly substitute $\mathbf{p}^2 \rightarrow (\mathbf{p} + \mathbf{k})^2$. This leads to the following equation for $|u_n^k\rangle$:

$$E_n |u_n^k\rangle = (V_0 + V_1 + V_2 + V_3) |u_n^k\rangle \quad (1.3)$$

$$V_0^k = \frac{\mathbf{p}^2}{2m} - eV + \frac{\hbar^2 k^2}{2m} \quad (1.4)$$

$$V_1^k = \hbar \frac{\mathbf{k} \cdot \mathbf{p}}{m} \quad (1.5)$$

$$V_2^k = -\lambda \boldsymbol{\sigma} \cdot (\nabla V \times \mathbf{k}) \quad (1.6)$$

$$V_3^k = -\lambda \boldsymbol{\sigma} \cdot (\nabla V \times \mathbf{p}). \quad (1.7)$$

We neglected the last two terms of Eq. 1.2 since they are exceedingly small and don't contribute to the linear form of Eq. 1.1.

Before turning to a $\mathbf{k} \cdot \mathbf{p}$ perturbative expansion of the above equations, we would like to address the question of which electric fields ∇V will contribute to V_2 and V_3 , i.e. that the former is the well-known first-order Rashba-Bychkov term, whereas the latter represents the atomic SOC. Both terms originate from the partial application of the third contribution in Eq. 1.2. To do this, we separate ∇V into two contributions, one coming from the potential wells created by the atoms, and another originating from the internal field created by the ferroelectric polarization

(it is assumed that no external fields are applied):

$$\nabla V = \mathbf{E} = \mathbf{E}_{at} + \mathbf{E}_P \quad (1.8)$$

These contributions, together with the two parts of the Bloch functions (i.e. the cell periodic $u_n^k(\mathbf{r})$, and envelope function $e^{ik\cdot r}$) are pictorially shown in Fig. 1.2.

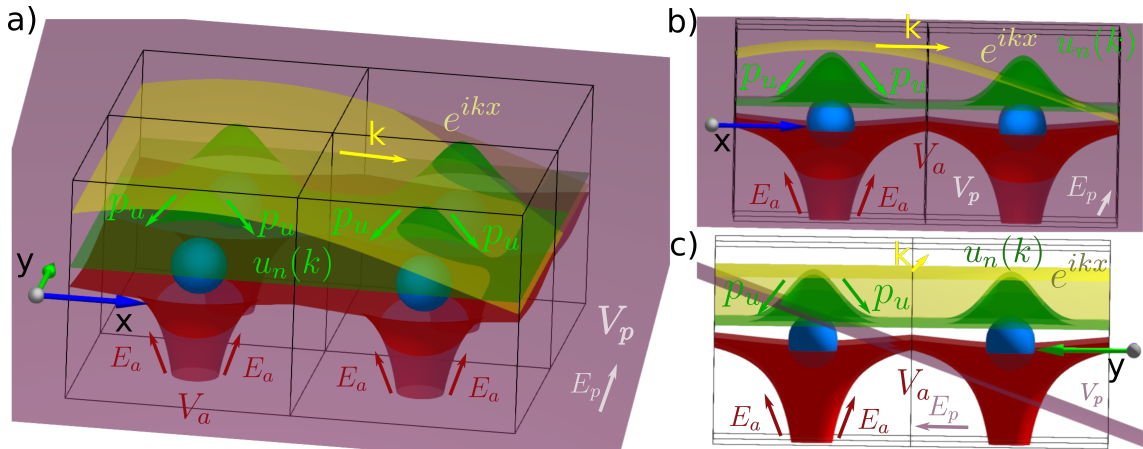


Figure 1.2: Pictorial representation of the different electric potentials (V) and fields (E) in a 2D square lattice. The blue spheres show the atoms, which produce the spherically symmetric red potential V_a and field E_a . The purple slab denotes a uniform ferroelectric polarization potential V_p which in this case is directed along the crystalline y -direction, creating field E_p . The green and yellow surfaces denote two components of the Bloch function: $u_n(k)e^{ikx}$, where the yellow is the envelope plane wave part and the green the cell periodic part. k and p_u denote the two components to the momentum of the bloch function, the former from the envelope function, and the latter the contribution from the periodic part.

Looking at the picture, it becomes clear that the contribution of the atomic potential applied to the envelope function is zero because while \mathbf{k} is a, \mathbf{E}_{at} is odd throughout the unit cell, leading to the contributions on either side of the potential wells to cancel out. Thus, the only contribution to V_2 comes from the uniform (even) \mathbf{E}_P , which is in general very small compared to the atomic one \mathbf{E}_{at} . A similar argument can be applied to the contribution to V_3 : due to the shape of the periodic part of the wavefunction, necessarily having zero total \mathbf{p}^2 , only the contribution from \mathbf{E}_{at} will be nonzero. This is essentially the well-known atomic SOC and can be rather large due to the large fields close to the ions.

We now turn to a perturbative expansion around a high-symmetry, time reversal (TR) invariant point \mathbf{k}_0 inside the first BZ. It is assumed that Eq. 1.3 can be solved for such a point, and where the two spin states are necessarily degenerate due to the TR symmetry. Due to the broken inversion symmetry and inclusion of the SOC terms (V_2, V_3), this degeneracy will be lifted for \mathbf{k} -points which are not TR

²The system would not be in an equilibrium state if the periodic part had nonzero momentum.

invariant. We denote the periodic parts of the two degenerate Bloch states by $|u_n^\downarrow\rangle$ and $|u_n^\uparrow\rangle$. It is important to realize that the orientation of spin axis of the eigenstates of Eq. 1.3 depends on the direction of both \mathbf{k} and \mathbf{P} , as will become clear later. This means that for each \mathbf{k} point, the actual orientation of the up and down spins varies. Without loss of generality we take $\mathbf{k}_0 = \mathbf{0}$ and $E_n^{\uparrow\downarrow}(\mathbf{0}) = 0$. Expanding in the deviation away from the high-symmetry point, in the usual $\mathbf{k} \cdot \mathbf{p}$ sense, and keeping only linear \mathbf{k} terms, and terms up to second order in $1/c$, we get

$$E_n^{\sigma_1}(\mathbf{k}) = -V_2^{\sigma_1}(\mathbf{k}) + \quad (1.9)$$

$$\sum_{m,\sigma_2 \neq n,\sigma_1} \frac{\langle u_n^{\sigma_1} | V_1(\mathbf{k}) | u_m^{\sigma_2} \rangle \langle u_m^{\sigma_2} | V_3(\mathbf{k}) | u_n^{\sigma_1} \rangle + h.c.}{E_n^{\sigma_1} - E_m^{\sigma_2}}. \quad (1.10)$$

Referring back to the earlier discussion on the origin of various terms in Eq. 1.3, and in particular what fields contribute to V_2 or V_3 , we find that, if u_n and u_m have contributions that originate from an atom with a strong SOC, the first and second term contribute with the same order of magnitude. This is true even though the latter is of higher order in the perturbation theory.

From the point of view of symmetries, another requirement for the second term to be nonzero is that u_n and u_m have contributions with different parity, since \mathbf{p} is odd in spatial coordinates, $\mathbf{k} \cdot \mathbf{p}$ is only non-zero when one of the constituent orbitals is odd with respect to a spatial direction and the other even. One example could be a p_y orbital and a $s-p_z$ hybridized one, which would be created by the ferroelectricity with electric polarization along the z -axis. This hybridization will be discussed in further detail in the context of a toy Tight-Binding model below.

We can thus arrive to the conclusion that, while these contributions are allowed and therefore present in inversion broken systems, they will contribute very little to the linear spin splitting due to the tiny prefactors (i.e. $\lambda \approx 10^{-6}$ eV) involved. It was thought for a long time that at interfaces, where the uniform ∇V in V_2 can be relatively big, the spin-splitting could be explained from this purely relativistic argument, but even there the contributions we discussed up to now are generally much smaller than what is observed in reality.

We thus need to seek a different explanation for the large splittings that are observed, especially for those in bulk materials, which brings us to the rest of this Chapter in which it will be shown that the combination of electrostatics with strong atomic SOC (V_3 in Eq. ??) can lead to the observed behavior. This will lead to a similar second order perturbative effect as in the second term of Eq. 1.9, but where the relativistic V_1 is substituted by a contribution from electrostatics, which is not plagued by the small relativistic prefactor.

1.3 Orbital Rashba Effect

As will be demonstrated throughout this section, it turns out that the key lies in the realization that Bloch functions at non-TR invariant k -points, generate nonzero in-

tercell electric dipoles if they have a nonzero orbital angular momentum (OAM)[**Petersen2000, Park2011, Go2016**]. These dipoles couple to any electric field, e.g. the internal one associated with ferroelectric polarization, with the inverse effect leading to the generation of Bloch functions with nonzero OAM. This OAM then couples to the spin of the electrons through the atomic SOC, leading to a splitting with the size determined (in part) by the weight of the ion around which the OAM develops. We will thus focus in this section on how this OAM appears, since it is well-known that in crystals it is generally said to be quenched. Indeed, ignoring atomic SOC, the influence of neighboring ions on the charge distribution of the atomic orbitals that form the Bloch functions is such that it favors orbitals with zero OAM. This is directly translated into the commonly used language of p_x , p_y and p_z orbitals in the case of $L = 1$.

Nonetheless, there exist two mechanisms that favor nonzero OAM. Firstly, atomic SOC gains energy through $\mathcal{H}_{SOC} = -\lambda_a \hat{\mathbf{L}} \cdot \hat{\boldsymbol{\sigma}}$ when the OAM is nonzero. Even at TR-invariant k -points this leads to orbitals with some OAM. When expanding for small \mathbf{k} , a linear varying term will appear in the energy dispersion that originates from the plane wave $e^{i\mathbf{k}\cdot\mathbf{r}}$ envelope of the Bloch functions. Secondly, even without inclusion of atomic SOC, it will be shown that the OAM of the Bloch functions appears in a chiral texture as one moves away from the high-symmetry k -point, similarly to how the relativistic Rashba effect leads to a chiral spin texture, due to the earlier discussed intercell dipoles. If one then includes again the atomic SOC, this linear-in- k \mathbf{L} results in a linear variation of the energy with either positive or negative slope depending on the spin orientation in relation to $\hat{\mathbf{L}}$.

We now proceed by giving a pedagogical derivation of these mechanisms based on a tight-binding model [**Petersen2000, Go2016**].

1.3.1 Tight-Binding model

The tight-binding model is defined on a 2D square layer with lattice parameter a , one atom per unit cell, and four Wannier orbitals centered on that atom. These orbitals resemble the angular character of an s -orbital and three p -orbitals: $|s^{\mathbf{n}}\rangle$, $|x^{\mathbf{n}}\rangle$, $|y^{\mathbf{n}}\rangle$, $|z^{\mathbf{n}}\rangle$, where \mathbf{n} denotes the unit-cell indices (n_x, n_y) to which the Wannier function belongs to. To simplify notation, we omit $\mathbf{0}$ in writing the Wannier functions of the central unit cell. We furthermore assume that these orbitals have a Gaussian radial shape $\langle \mathbf{r}|s_{\mathbf{n}}\rangle = e^{-\frac{|\mathbf{r}-\mathbf{n}a|^2}{a_0}}$, $\langle \mathbf{r}|\alpha_{\mathbf{n}}\rangle = \alpha e^{-\frac{|\mathbf{r}-\mathbf{n}a|^2}{a_0}}$ with $\alpha = x, y, z$, and inner products implying integrals over space. The reason for choosing gaussians is to make solving the overlap integrals easier, changing to a different radial shape for the orbitals does not lead to any qualitative changes to the derivation below. The bare tight-binding Hamiltonian is denoted as \hat{H}_0 and includes the usual hopping parameters due to overlap $t_{\alpha\beta}^{\mathbf{n}\mathbf{n}'} = \langle \alpha^{\mathbf{n}} | \frac{\hat{\mathbf{p}}^2}{2m} + \hat{V} | \beta^{\mathbf{n}'} \rangle$. To mimick the inversion symmetry breaking in ferroelectric materials (i.e. with a polar space group), an electric field perpendicular to the layer (z direction) is applied. This allows extra hopping terms associated

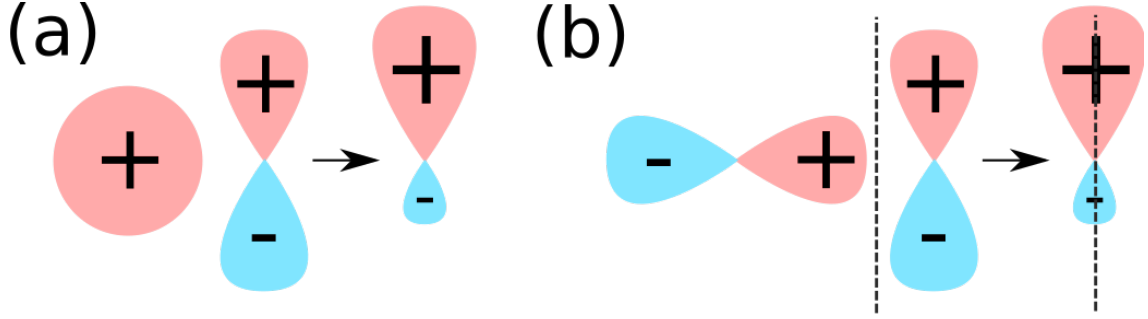


Figure 1.3: **Overlap dipoles.** (a) On-site dipole from $|s\rangle$ and $|z\rangle$ hybridization, (b) Dipole due to overlap of shifted $|p\rangle$ orbitals, the dashed line signifies a unit cell boundary.

with $\hat{H}_{isb} = e(\hat{\mathbf{d}} \cdot \mathbf{E})$, with $\hat{\mathbf{d}}$ the electric dipole moment:

$$\langle s | \hat{H}_{isb} | z \rangle = 2eE_z\theta_z^0 \quad (1.11)$$

$$\langle z | \hat{H}_{isb} | x^n \rangle = eE_z\theta_z^n n_x \quad (1.12)$$

$$\langle z | \hat{H}_{isb} | y^n \rangle = eE_z\theta_z^n n_y \quad (1.13)$$

with $\theta_z^n = -ae^{-\frac{1}{2}\left(\frac{a|\mathbf{n}|}{a_0}\right)^2} \frac{\pi^{\frac{3}{2}}}{16\sqrt{2}}$, other terms of \hat{H}_{isb} are zero. Fig. 1.3 shows pictorially how these terms arise from the electric dipoles between the shifted orbitals. Since we are interested in ferroelectric materials, the internal field E_z caused by the electric polarization is usually small. This warrants a perturbative approach where \hat{H}_{isb} is the perturbation on \hat{H}_0 , leading to a hybridization between the $|s\rangle$ and $|z\rangle$ orbitals:

$$|\tilde{z}\rangle = |z\rangle + \frac{\langle s | 2eE_z\theta_z^n | z \rangle}{\varepsilon_z - \varepsilon_s} |s\rangle \quad (1.14)$$

$$|\tilde{s}\rangle = |s\rangle + \frac{\langle z | 2eE_z\theta_z^n | s \rangle}{\varepsilon_s - \varepsilon_z} |z\rangle, \quad (1.15)$$

where $\varepsilon_s = \langle s | \hat{H}_0 | s \rangle$ and $\varepsilon_z = \langle z | \hat{H}_0 | z \rangle$.

We can then write the kinetic energy part of \hat{H}_0 and terms of this hybrid $|\tilde{z}\rangle$ orbital in the central unit cell and the shifted $|x\rangle$, $|y\rangle$ orbitals, leading to:

$$\langle \tilde{z} | \hat{H}_0 | x^n \rangle = \frac{2eE_z\theta_z^n}{\varepsilon_z - \varepsilon_s} \langle s | \frac{-\nabla^2}{2} | x^n \rangle \quad (1.16)$$

$$= \frac{4eE_z(\theta_z^n)^2}{\varepsilon_z - \varepsilon_s} n_x (-5 + a^2 |\mathbf{n}|^2) \quad (1.17)$$

$$\langle \tilde{z} | \hat{H}_0 | y^n \rangle = \frac{4eE_z(\theta_z^n)^2}{\varepsilon_z - \varepsilon_s} n_y (-5 + a^2 |\mathbf{n}|^2) \quad (1.18)$$

To construct \hat{H}_0^k and \hat{H}_{isb}^k , one can fourier transform the Wannier Functions following Eq. ??:

$$|\alpha^k\rangle = \frac{1}{\sqrt{N}} \sum_{\mathbf{n}} e^{i\mathbf{k}\cdot\mathbf{n}} |\alpha^n\rangle \quad (1.19)$$

with $|\alpha\rangle$ one of the four aforementioned orbitals, \mathbf{k} written in terms of crystalline coordinates ($\frac{2\pi}{a}$), and N denoting the total amount of unit cells in the material. This results in:

$$\hat{H}_0^{\mathbf{k}} + \hat{H}_{isb}^{\mathbf{k}} = \sum_{\mathbf{n}} e^{i\mathbf{k}\cdot\mathbf{n}} (\hat{H}_0^{\mathbf{n}} + \hat{H}_{isb}^{\mathbf{n}}) \quad (1.20)$$

If we then assume that at $k = 0$ the Bloch functions are formed from p_x , p_y , \tilde{p}_z and \tilde{s} orbitals through Eq. 1.19, a perturbation theory for small deviations \mathbf{k} away from zero can be formulated as ($\mathbf{k} = 0$ superscripts are omitted for simplicity):

$$|\alpha^{\mathbf{k}}\rangle = |\alpha\rangle + \sum_{\beta \neq \alpha} \frac{\langle \beta | \hat{H}_0^{\mathbf{k}} + \hat{H}_{isb}^{\mathbf{k}} | \alpha \rangle}{\varepsilon_{\alpha} - \varepsilon_{\beta}} |\beta\rangle \quad (1.21)$$

Gathering the linear-in- k terms from the expansion of $e^{i\mathbf{k}\cdot\mathbf{n}}$ in Eq. 1.20, and assuming $\varepsilon_p = \langle x | \hat{H}_0 | x \rangle = \langle y | \hat{H}_0 | y \rangle$ at $\mathbf{k} = 0$, we find

$$|x^{\mathbf{k}}\rangle = |x\rangle + i\Theta \frac{k_x}{\varepsilon_p - \varepsilon_{\tilde{z}}} |\tilde{z}\rangle \quad (1.22)$$

$$|y^{\mathbf{k}}\rangle = |y\rangle + i\Theta \frac{k_y}{\varepsilon_p - \varepsilon_{\tilde{z}}} |\tilde{z}\rangle \quad (1.23)$$

$$|\tilde{z}^{\mathbf{k}}\rangle = |\tilde{z}\rangle + i\Theta \frac{1}{\varepsilon_{\tilde{z}} - \varepsilon_p} (k_x |x\rangle + k_y |y\rangle), \quad (1.24)$$

with $\Theta = \frac{\pi^{5/2}}{256a^3} \left(-16\sqrt{2} + \frac{3a\pi^{3/2}}{\varepsilon_z - \varepsilon_s} \right) eE_z$. Then, using the definition of the OAM operators for p -orbitals:

$$\hat{L}_x = \begin{pmatrix} 0 & 0 & 0 \\ 0 & 0 & -i \\ 0 & i & 0 \end{pmatrix}, \hat{L}_y = \begin{pmatrix} 0 & 0 & i \\ 0 & 0 & 0 \\ -i & 0 & 0 \end{pmatrix}, \hat{L}_z = \begin{pmatrix} 0 & -i & 0 \\ i & 0 & 0 \\ 0 & 0 & 0 \end{pmatrix} \quad (1.25)$$

we find that,

$$\langle \tilde{z}^{\mathbf{k}} | \hat{L}_x | \tilde{z}^{\mathbf{k}} \rangle = -2\Theta \frac{k_y}{\varepsilon_{\tilde{z}} - \varepsilon_p} \quad (1.26)$$

$$\langle \tilde{z}^{\mathbf{k}} | \hat{L}_y | \tilde{z}^{\mathbf{k}} \rangle = 2\Theta \frac{k_x}{\varepsilon_{\tilde{z}} - \varepsilon_p} \quad (1.27)$$

These expressions for $\hat{\mathbf{L}}$ can be filled into the expression for the atomic SOC $\hat{H}_{soc} = \lambda \hat{\mathbf{L}} \cdot \hat{\boldsymbol{\sigma}}$ to find the energy for $|\tilde{z}^{\mathbf{k}}\rangle$:

$$\varepsilon^{\mathbf{k}} = \frac{2\lambda\Theta}{\varepsilon_{\tilde{z}} - \varepsilon_p} (\mathbf{k} \times \boldsymbol{\sigma}) \quad (1.28)$$

which has the form of Eq. 1.1. We want to emphasize here that the only influence of the initial choice of the Gaussian radial shape of the orbitals is reflected in the prefactor in front of eE_z in the definition of Θ .

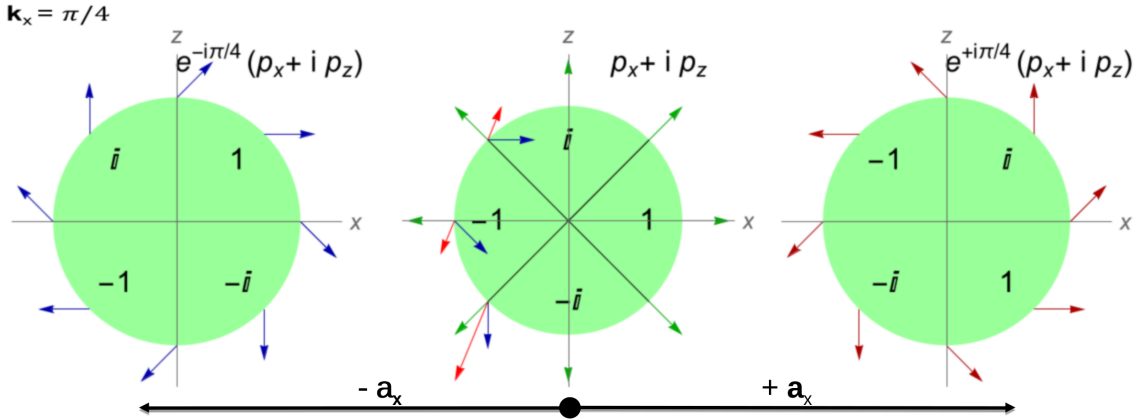


Figure 1.4: Interference between orbitals with nonzero OAM. Three neighboring unit cells are displayed, each with the same $p_x + ip_z$ orbital (thus having nonzero l_y). The wave functions of the left and right unit cells have their phase rotated by the plane-wave part $e^{ik_x R_x}$. The amplitude and phase of the wave function are encoded with the length and polar angle of the arrows. It is clear from the resulting phases (red arrows) that there exists constructive interference on the bottom half of the material, and destructive interference at the top half, which leads to the intercell dipoles.

From this qualitative derivation, it is clear that the main reason behind the orbital Rashba effect can be traced back to the observation that Bloch functions with nonzero OAM have electric dipoles that couple to the inversion symmetry breaking electric field. We identified two sources that lead to the effect.

The first one comes from the direct overlap dipoles between p_x and p_y orbitals with the p_z orbital (panel (b) in Fig. 1.3)[**Petersen2000**]. An exaggerated demonstration for the case of $p_x + ip_z$ orbitals is shown in Fig. 1.4.

The second is due to the hybridization of the s and p_z orbitals (panel (a) in Fig. 1.3), and the kinetic energy term between the s and neighboring p_x and p_y orbitals[**Go2016**]. These two terms are reflected in the two terms that contribute to Θ , and lead to a chiral, linear-in- k texture of the OAM. Through the atomic SOC, this linear-in- k OAM will couple to the spin and result in the final splitting with the Rashba-like form of Eq. 1.28.

There is one final term that contributes to the linear variation of OAM with \mathbf{k} , which is present due to the unquenching of the OAM at the high symmetry point (e.g. $|\mathbf{k}| = 0$) due to atomic SOC ???. If the Bloch functions at $\mathbf{k} = 0$ are written as a linear combination of Wannier functions that have angular character of p -orbitals

$$|\psi\rangle = \sum_{\mathbf{n}, \alpha} c_\alpha |\alpha^\mathbf{n}\rangle, \quad (1.29)$$

the general formula for the OAM in terms of these c_α becomes

$$\hat{L}_\gamma = i\epsilon_{\alpha\beta\gamma} c_\alpha^* c_\beta \quad (1.30)$$

when α, β, γ designate x, y, z . Thus, through the gain on \hat{H}_{soc} if $\mathbf{j} = \mathbf{l} + \boldsymbol{\sigma}$, the orbitals at the high-symmetry point will now be a linear combination of what were originally pure p -orbitals (due to the quenching we assumed that the bands at $\mathbf{k} = 0$ had a single $c_\alpha \neq 0$ in the previous derivation). This unquenching will not be complete in the sense that it won't create orbitals with maximal \mathbf{j} as is the case for an isolated ion through the Hund's rules, since in a crystal the neighboring charge will limit the creation of OAM³.

Similar to the above derivation, a small- k expansion for Bloch functions $|\psi^k\rangle$ with nonzero OAM can be performed around $|k| = 0$ leading in general to:

$$|\psi^k\rangle = \sum_{\mathbf{n}, \alpha} c_\alpha^k e^{i\mathbf{k}\cdot\mathbf{n}} |\alpha^n\rangle \quad (1.31)$$

$$= \sum_{\mathbf{n}, \alpha} \left(c_\alpha + \mathbf{k} \frac{\partial c_\alpha^k}{\partial k} \Big|_{\mathbf{k}=0} \right) (1 + i\mathbf{k}\cdot\mathbf{n}) |\alpha^n\rangle. \quad (1.32)$$

Again we omit terms with $\mathbf{k} = 0$ for clarity. Focusing on the terms that vary linearly with k , the second term in the c_α expansion together with the first term in the exponent expansion is exactly the contribution that was discussed before. The other term for the Orbital Rashba effect, due to unquenching, originates from combining the first term in the c_α expansion with the second in the exponent expansion, leading to the contribution

$$\varepsilon^k = \langle \psi^k | \hat{H}_{isb} | \psi^k \rangle = i \sum_{\mathbf{n}, \alpha, \beta} c_\alpha^* c_\beta \mathbf{k} \cdot \mathbf{n} \langle \alpha | \hat{H}_{isb} | \beta^n \rangle \quad (1.33)$$

$$= \frac{-\pi^{5/2}}{8\sqrt{2}a^3} i(c_x^* c_z k_x + c_y^* c_z k_y) e E_z \quad (1.34)$$

$$= \frac{\pi^{5/2}}{8\sqrt{2}a^3} (L_y k_x - L_x k_y) e E_z. \quad (1.35)$$

These expressions show us that, due to $\hat{H}_{soc} = \lambda \hat{\mathbf{L}} \cdot \hat{\boldsymbol{\sigma}}$ and $\hat{H}_{isb} = e E_z d_z$, an additional Rashba-like term appears in the energy dispersion, due to the creation of orbitals with nonzero L_y and L_x at the high-symmetry point.

With the understanding that one can find Rashba like dispersions, coming not from the usually considered purely relativistic, but also from electrostatic mechanisms, we now look at a concrete example that behaves very similar to the above toy model, GeTe.

1.4 Germanium Telluride

At high temperatures GeTe has the standard rocksalt structure. When temperatures are lowered, a displacive phonon instability occurs, freezing in a $\mathbf{q} = 0$ phonon that shifts the central Te ion along the [111] direction[Rabe1987]. The space group after

³This is the reason why without SOC the OAM is fully quenched.

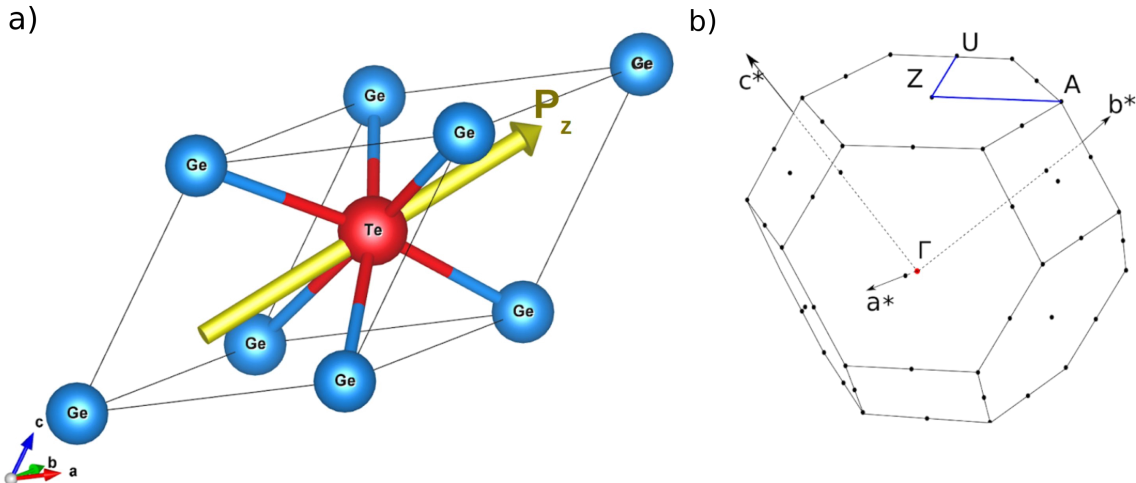


Figure 1.5: **Crystal structure of GeTe**(a) Rhombohedral unit cell, with the polarization along the [111] direction in yellow. b) First Brillouin zone with the high-symmetry k -path that is under focus indicated by the blue lines.

this inversion symmetry breaking phase transition becomes $R\bar{3}m$ (#160 in International Tables), and a nonzero electric polarization along the z -direction develops as indicated by the yellow arrow in Fig. 1.5(a). The first BZ for this low temperature structure is shown in panel (b), with the high-symmetry path under focus indicated by the blue line.

The valence and conduction bands are formed mostly by s - and p -orbitals from the Te and Ge ions, respectively, as can be seen from Fig. 1.6. From the fully relativistic bandstructure in panel (b) it can be seen that multiple bands exhibit a large linear spin splitting around the Z -point in the plane perpendicular to the [111] direction. The $Z - \Gamma$ path does not show any splitting because the electric field

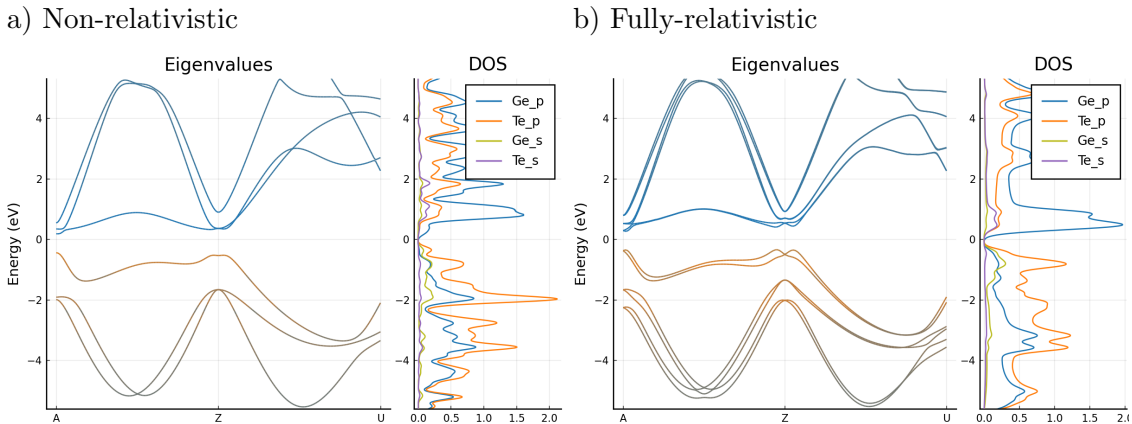


Figure 1.6: **Bandstructure of GeTe** In both panels the bandstructure was colored according to the contribution of the constituent orbitals, as indicated in the flanking density of state plots. The bands that have larger s character are situated 5 eV below the shown window.

is along the z -direction, and thus only a variation of k_x and k_y will show a linear splitting, as previously discussed.

This means that from the point of view of our earlier derivation using the tight-binding model in terms of s - and p -orbitals, it is the perfect test case. Moreover, since it is a bulk material, we can neglect the contributions from to the relativistic Rashba effects described in Sec. 1.2, due to the small potential gradients ∇V resulting from the bulk ferroelectricity.

1.5 Methods

In order to study this effect in a quantitative manner, without relying on experiments to fit the model to, the bandstructure is simulated from first-principles. Density functional theory (DFT), originally envisioned in the seminal works of P. Hohenberg, W. Kohn and L. J. Sham [**Hohenberg1964**, **Kohn1965**], is a formalism very well suited for achieving this goal. We won't delve into the fine details in light of conciseness, resorting instead to a very high-level overview following the excellent introduction to the topic by R. Martin in Ref. [**Martin2004**]. On a rudimentary level, DFT is built on top of three main theoretical pillars.

The first pillar is the observation that any property of a system of interacting particles can be written as a functional of the ground-state density $n_0(\mathbf{r})$. This means that DFT is, in principle, an exact theory of many-body systems. Writing the Hamiltonian as

$$\hat{\mathcal{H}} = -\frac{\hbar}{2m_e} \sum_i \nabla_i^2 + \sum_i V_{\text{ext}}(\mathbf{r}_i) + \frac{1}{2} \sum_{i \neq j} \frac{e^2}{|\mathbf{r}_i - \mathbf{r}_j|}, \quad (1.36)$$

where the indices i, j iterate over the electrons⁴, the statement is that V_{ext} is uniquely defined by $n_0(\mathbf{r})$, and vice versa. Thus, as soon as the ground-state density is found, the exact Hamiltonian of the system is known. This in turn allows one to find all other eigenstates of the system, exactly solving the problem in the process.

The second pillar is formed by the ability to define a universal functional for the total energy of the system $E[n]$ in terms of the density $n(\mathbf{r})$, which is valid for any external potential V_{ext} . The density that globally minimizes this functional is then equal to the ground-state density $n_0(\mathbf{r})$.

In order to turn these foundational first two pillars into a practically usable framework, one needs to address the question of the form of the energy functional $E[n]$, leading us straight to the third pillar: the Kohn-Sham Ansatz [**Kohn1965**]. In essence, this ansatz makes the assumption that the original many-body problem can be replaced by an auxiliary independent-particle problem, both having exactly the same ground-state density $n_0(\mathbf{r})$. This means that, theoretically speaking, calculations for the many-body problem can be exactly translated instead into calculations

⁴The ionic terms are easily included and are not the core difficulty and thus omitted here.

using independent-particle methods. It is found that a set of independent particle equations can thus be formulated, lumping all the cumbersome many-body terms together in the so-called “exchange-correlation” functional $E_{xc}[n]$. If the exact form of $E_{xc}[n]$ was known, DFT would lead to the exact solutions of the original many-body problem. The success of the DFT method from a numerical and quantitative point of view can be wholly attributed to the ability of finding local or semi-local approximations to this functional that manage to often reproduce quite well, in a mean-field kind of way, the original many-body problem.

Bringing everything together, we can write down the total energy functional as:

$$E_{KS} = T_s[n] + \int d\mathbf{r} V_{\text{ext}}(\mathbf{r}) n(\mathbf{r}) + E_{\text{Hartree}}[n] + E_{II} + E_{xc}[n], \quad (1.37)$$

where T_s is the independent-particle kinetic energy, V_{ext} the external potential due to the nuclei and any other external fields, E_{II} the Coulomb interactions between the nuclei, and $E_{\text{Hartree}}[n]$ denoting the classical Coulomb contributions:

$$E_{\text{Hartree}} = \frac{1}{2} \int d\mathbf{r} d\mathbf{r}' \frac{n(\mathbf{r}) n(\mathbf{r}')}{|\mathbf{r} - \mathbf{r}'|}. \quad (1.38)$$

The next question is how to perform the minimization in order to find the ground-state density n_0 . In general, a self-consistent algorithm is used that iteratively constructs the energy contributions from the previous trial density n_i , diagonalizes the resulting Hamiltonian, and uses the found ground-state wavefunction to construct a new trial density n_o , after which the algorithm is repeated until n_o is sufficiently close to n_i . This means that the energy terms which, according to the Hohenberg-Kohn theorems are uniquely defined by the density, did not change markedly w.r.t. the previous iteration, i.e. self-consistency between density and functional is reached. It can be shown that this process, at least, leads to a local minimum of the Kohn-Sham functional^{1.37}. The question of how to reach the global minimum of any function, let alone any functional, is from an entirely different caliber that we wish to avoid in this thesis.

There are many ways to numerically implement DFT, with variations depending mostly on the basis set of independent particle that is being used to construct the energy functional. Since we are interested in extended systems such as crystals, a plane-wave basis set comes very natural. In this case, both the envelope and unit-cell periodic part of the Bloch functions $|\psi^{\mathbf{k}}\rangle = e^{i\mathbf{k}\cdot\mathbf{r}} |u^{\mathbf{k}}\rangle$ are represented in terms of plane waves.

In the calculations presented here, we used the implementation in the Quantum ESPRESSO software package[**Giannozzi2009**]. To limit the size of the plane wave basis set that needs to be used, this package uses another approximation: the so-called Pseudopotentials that replace the exact ionic potentials. Again, a full description of pseudopotentials is out of scope of this thesis, but the main point is that they try to alleviate the requirement of including very fast oscillating plane waves (very high energy) in order to resolve the fast density oscillations that occur

close to the ionic cores. Indeed the atomic states out of which Bloch functions are formed usually have one or many nodes close to the ionic cores. Pseudopotentials define a different potential for those cores in such a way that the wavefunctions match identically the exact ones outside the core region, but have less nodes and therefore a smoother density variation close to the cores. In most problems one is not interested in the exact form of the wavefunctions close to the core anyway.

In order to confirm the linear varying OAM even when spin-orbit is not included we performed non-relativistic, as well as fully relativistic DFT calculations. Both were performed using the Optimized Norm-conserving Vanderbilt Pseudo Potentials [**Hamann2013**], a generalized-gradient approximation for the exchange-correlation functional [**Perdew1996**]. Plane waves with an energy cutoff of 30 Ry were included, with a 120 Ry cutoff for the density.

The reciprocal space was sampled using a 6x6x6 Monkhorst-Pack grid [**Pack1977**] for the self-consistent calculation, using a total energy convergence threshold of 10^{-7} Ry.

Afterwards we used the Wannier90 package [**Mostofi2014AnFunctions**] to perform the Wannierization as described in the theory Chapter ??, using projections on hydrogenic *s*- and *p*-orbitals for both Ge and Te ions as the initial guess. A 10x10x10 *k*-grid was used for the sampling of the BZ during the Wannierization. The result is shown in Fig. 1.7.

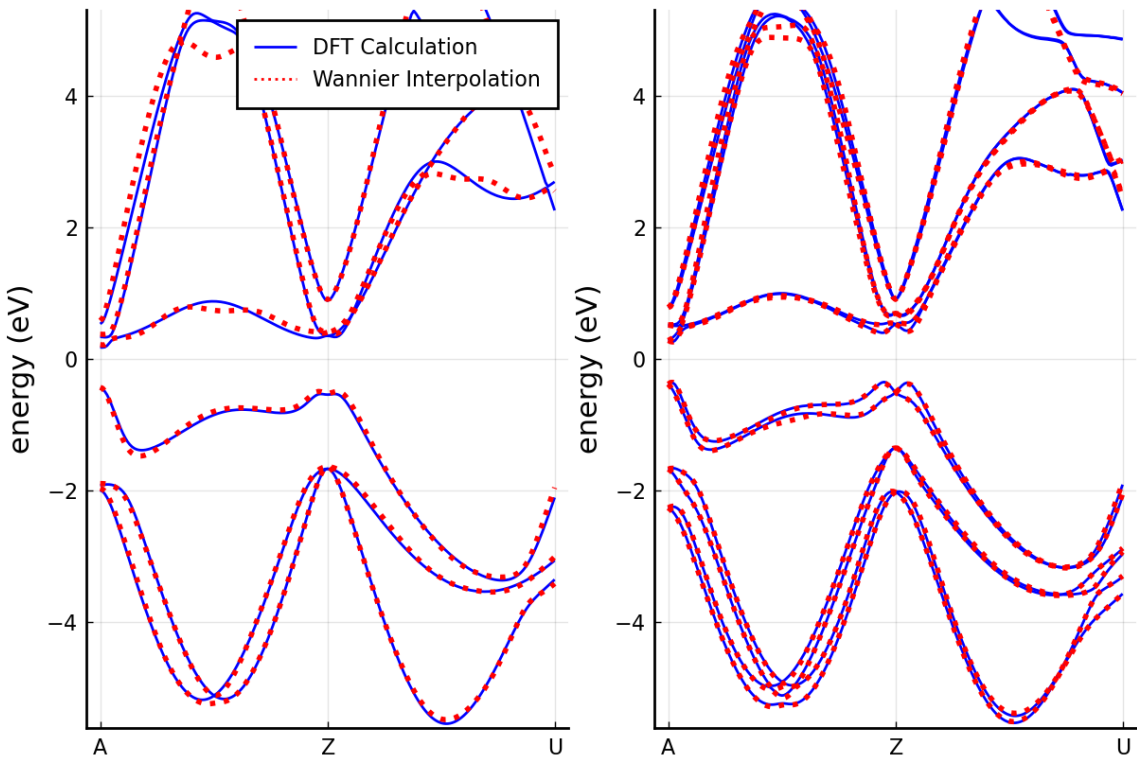


Figure 1.7: Result of Wannierization procedure for non-relativistic (a) and relativistic (b) calculations.

[look in the high throughput paper for a decent definition of the wannier band distance w.r.t the dft one!]

1.6 Results and Discussion

The bands we will focus on most are the three topmost valence bands. As seen in Fig. ??-(b), these bands have the largest spin-splitting. This suggests that indeed the atomic SOC plays an important rule, seen as these bands are comprised mostly of Te orbitals, and SOC is largest on Te. If one were to fit the dispersion of the topmost band to Eq. 1.1, it results in a large prefactor $\alpha_R \approx 30.7 \text{ eV}\cdot\text{\AA}$ [DiSante2013]. As discussed before, a more realistic prefactor would be $\alpha_R = 10^{-6} \text{ eV}$ in the purely relativistic case inside the vacuum.

The last issue with the purely relativistic explanation, which has been confirmed experimentally[Krempasky2015SurfaceSemiconductor], lies in the orientation of the spin polarization of the split bands. According to Eq. 1.1, the bands should all be split equally and Bloch functions at the same k -point should have the same spin orientations, since their character does not enter Eq. 1.1. However, as has been shown and will be confirmed by our results below, the orientation depends on the character of the band, more specifically on the value of the total angular momentum j .

[also put some values on the wannier centers etc] The dispersion, OAM, and SAM of the first valence band are shown in the left panel of Fig. 1.8. Confirming our earlier conclusions, we can see that non-zero, linearly varying OAM is formed as we move away from the high-symmetry Z -point. Moreover, the OAM is perpendicular to both the z -axis and the k vector, as it should be from Eq. 1.26, and can also be seen from the panels in Fig. 1.10. This leads e.g. to $l_y = 0$ along the $A \rightarrow Z$ path, where only k_y is nonzero. When atomic SOC is included in the orange and blue graphs, we see the spin-splitting that results from having the spin oriented either along or opposite to the already linearly varying OAM. The unquenching of the OAM at the Z -point when SOC is included is also clearly visible, together with the resulting change in the slope that originates from the corresponding contribution to the dipole moment Eq. 1.33. This correlation can also be observed in the panel showing the center of mass $\bar{z} = \int_{\text{supercell}} z|\psi(k)|^2$ of the Bloch-functions, which is proportional to the dipole moment around the same reference point.

When we compare this first valence band with the third valence band, shown in the right panel of Fig. 1.8, we can clearly see the previously discussed issues with the purely relativistic explanation. As stated before, we can note that not only the magnitude but also the sign of the prefactor in Eq. 1.1 is opposite for these two bands, showcased by the size of the splitting, and by the ordering of the spin-up vs the spin-down splitted part. This is because the character of the first and third valence bands are different. The first valence band is mostly coming from Te $j_{\frac{3}{2}}$ orbitals, whereas the third valence band is predominantly $j_{\frac{1}{2}}$. This causes

the orientation of the OAM and SAM to be along each other in the first band, and opposite for the third, as shown in Fig. 1.10. This then leads to the different ordering of the spin-split bands.

There is one last very interesting feature one can notice from Fig. 1.10 (c) and (f), that is, the switching of the character (and SAM, OAM orientation) of the bands, very close to the Z point. This is because the crystal field breaks rotational symmetry causing the atomic j to not be a conserved quantity, i.e. there is a mixing between different atomic j orbitals, which varies strongly in this very narrow region around Z .

All these considerations lead to a very nontrivial SAM and OAM texture of the bands as we progress through the BZ.

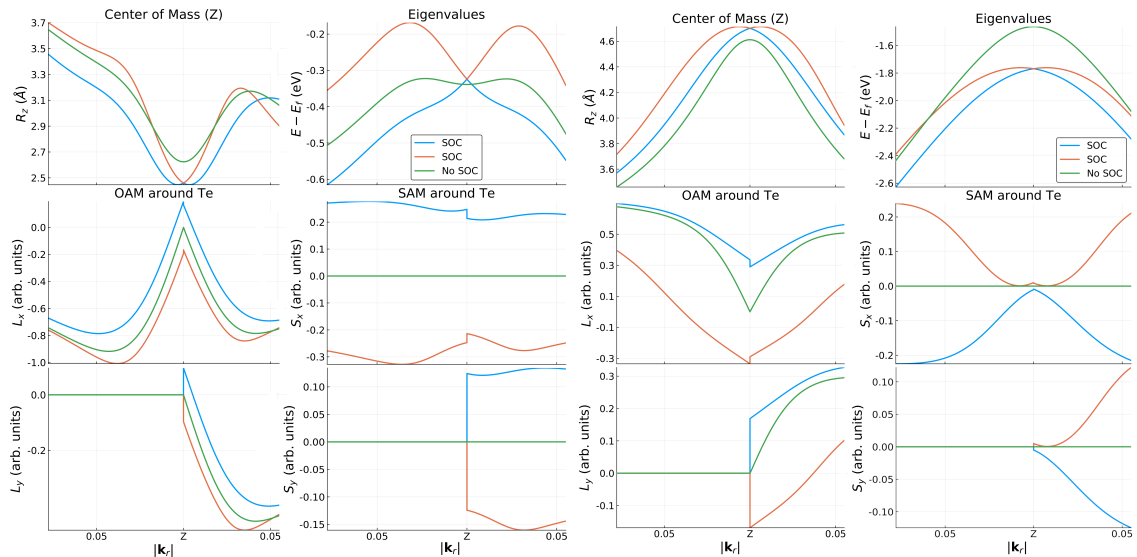


Figure 1.8: Comparison between the real-space observables and energy dispersion in (a) the first and (b) third valence band. The values are plotted in function of the relative distance from the Z point $\mathbf{k}_r = \mathbf{k} - \mathbf{k}_Z$, towards the A and U points. The green graphs denote the values before turning on atomic SOC, whereas the orange and blue graphs denote the two spin-split bands.

1.7 Conclusions

We have explored the microscopic origin of the giant Rashba-like spin splitting in the band structure of bulk ferroelectric GeTe with high atomic SOC. We derived the form of the band dispersion in the Wannier representation, that relates the large spin splitting to the intricate interplay between OAM, atomic SOC, the crystal field and the electric polarization. It turns out that the crucial component, which is not present in the relativistic Rashba effect, is the emergence of a nonzero electric dipole of the Bloch functions due to their OAM. The quantitative analysis based on Wannier functions and atomic-centered approximation confirms this mechanism

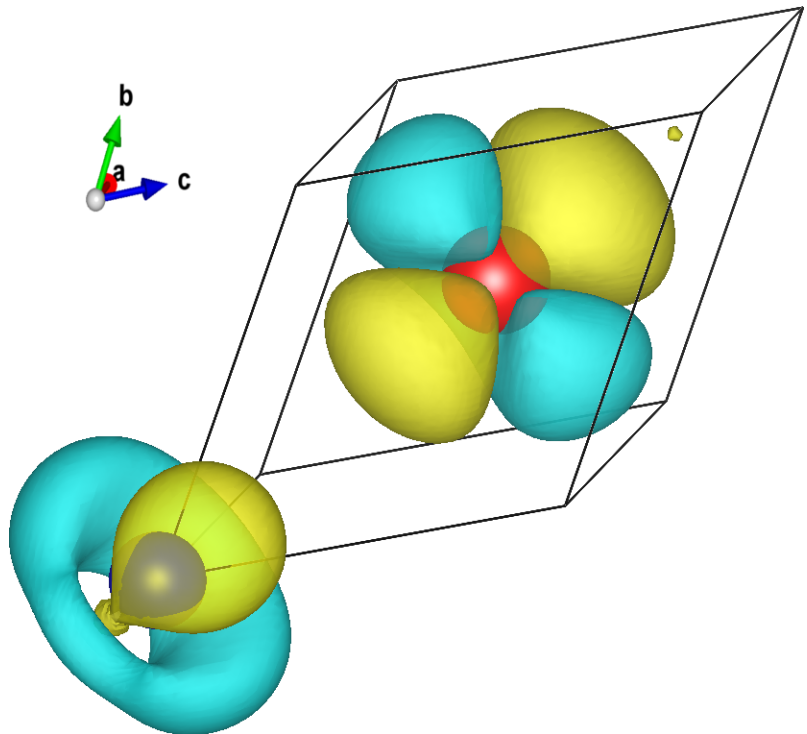


Figure 1.9: The variation of the charge density of the Bloch function of the first valence band $\frac{\partial|\psi(k)|^2}{\partial k}\Big|_{k=Z}$ away from Z towards A . Te and Ge ions are in red and blue, respectively. The charge asymmetry around Ge showcases the nonzero dipole moment along z , which couples to the local electric field near Ge ion.

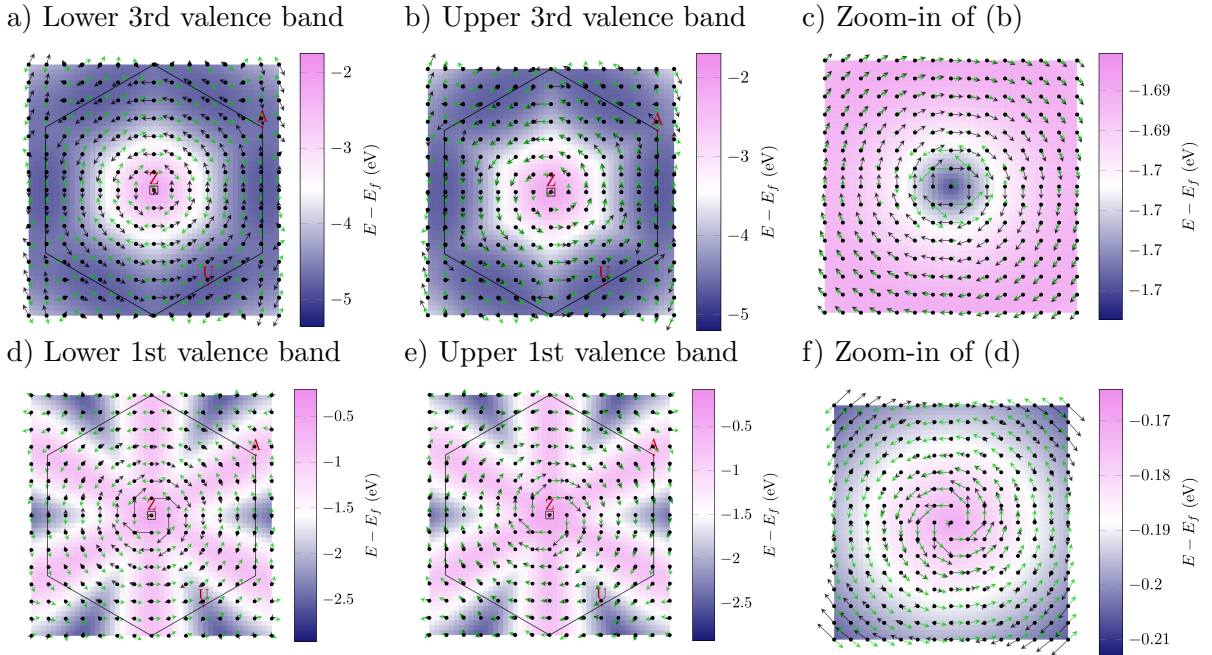


Figure 1.10: OAM and SAM textures around the Z point in the first and third valence bands of GeTe. The black and green arrows show the OAM and SAM textures, respectively. The length of the arrows was chosen separately for clarity in each figure and should thus not be compared. The color maps signify the energy of the bands, relative to the Fermi level. The small box around the Z point indicates the area, magnified in panels (c) and (f). In the zoomed figures (c) and (f) one can observe the change or relative orientation between the SAM and OAM when moving away from the Z point, signifying a change of character between $j = 1/2$ and $j = 3/2$.

in GeTe. We find a very good agreement between the proposed band dispersion, Eq. (??), and the dispersions of the first and third valence bands, where the effect manifests itself most clearly.

Ultimately, the results suggest that (1) large ferroelectric polarization, (2) high atomic SOC, and (3) highly symmetric environment producing little OAM quenching could be the design rules for new materials with strong Rashba-like spin splitting. These materials could enable spintronic devices with the much needed electric control of spin polarization.